PERGAMON

International Journal of Solids and Structures 40 (2003) 4813–4836

INTERNATIONAL JOURNAL OF SOLIDS and STRUCTURES

www.elsevier.com/locate/ijsolstr

Exact dynamic solutions to piezoelectric smart beams including peel stresses Part II: Numerical results, comparison and approximate solution

Quantian Luo, Liyong Tong *

School of Aerospace, Mechanical and Mechatronic Engineering, The University of Sydney, Bldg J11, Sydney, NSW 2006, Australia

Received 1 September 2002; received in revised form 28 April 2003

Abstract

This work presents numerical results for the exact dynamic solution of piezoelectric (PZT) smart beams including peel stresses, which was developed in Part I. Numerical results are presented in details for frequency spectra, natural frequencies, normal mode shapes, harmonic responses of the shear and peel stresses, and sensing electric charges for a cantilever beam with a bonded PZT patch to the clamped end. The exact dynamic solution can provide useful data for benchmarking other methods. The numerical results of the present model including peel stresses (PSM) are also compared with those obtained using the shear lag beam model and the shear lag rod model. On the basis of the equivalent forces derived in the static analysis, simple approximate dynamic solutions are obtained and compared with the exact solutions, and then the application and limitation of the simple approximate solutions are investigated. By comparing numerical results predicted by the present PSM model with the shear lag models and the approximate solutions based on the static equivalent forces, effects of the dynamic shear and peel stresses on natural frequencies and dynamic responses of the smart structures are examined.

Keywords: Smart beam; Dynamics; Shear and peel stresses; Piezoelectrics

1. Introduction

In Part I of this work (Tong and Luo, 2003), we developed the exact dynamic solutions for piezoelectric (PZT) smart beams including peel stresses and for the shear lag models. In this part, we present the numerical results for a cantilever beam with a bonded PZT patch to the clamped end as shown in Fig. 1, and compare the present PSM model with the shear lag models. Simple approximate dynamic solutions are developed and compared with the exact dynamic solutions including peel stresses. By comparing with the

* Corresponding author. Tel.: +61-293-516-949; fax: +61-293-514-841.
E-mail address: ltong@aeromech.usyd.edu.au (L. Tong).

0020-7683/03/$ - see front matter © 2003 Elsevier Ltd. All rights reserved.
doi:10.1016/S0020-7683(03)00246-4

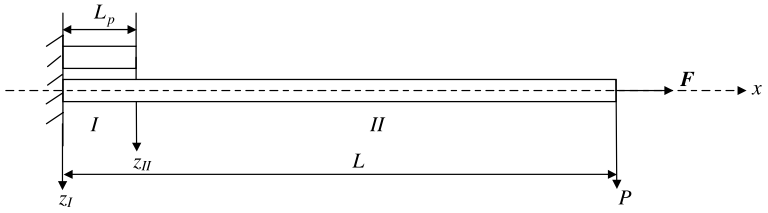

Fig. 1. A smart beam with one bonded PZT patch to the clamped end.

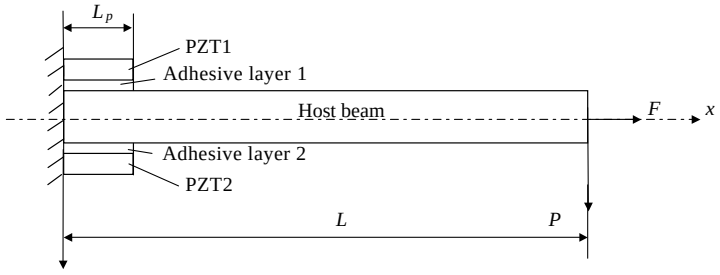

Fig. 2. A smart beam with two symmetrically bonded PZT patches.

exact dynamic solution of the shear lag rod model (SLRM) for smart beams shown in Figs. 1 and 2, limitations of the approximate dynamic solutions based on equivalent forces derived using PSM and SLRM are investigated. The following data are used to compute the numerical results except for the particular indication:

PZT patches: $E_1 = 7 \times 10^{10}$ N/m^2, $e_{31} = -5.2$ N/(mv), $t_1 = 0.001$ m, $L_p = 0.02$ m, $\rho = 7800$ kg/m^3.
Adhesive layers: $E_a = 3 \times 10^9$ N/m^2, $G_a = 1.07 \times 10^9$ N/m^2, $t_a = 0.0001$ m.
Host beam: $E_h = 7 \times 10^{10}$ N/m^2, $h = 0.001$ m, $\rho = 7800$ kg/m^3, $L = 0.2$, 0.6 m.

The above given data may represent properties of typical piezoceramics and epoxy resin. Definitions of all mathematical symbols are the same as those in Part I (Tong and Luo, 2003). The smart beam used for calculating the numerical results is shown in Figs. 1 and 2.

The exact dynamic solutions given in Part I (Tong and Luo, 2003) are expressed in a closed form of the steady state motion equations rather than in a Fourier series form. The frequency spectra are firstly presented, and then the resonant frequencies or natural frequencies are determined based on the frequency spectra. The normal mode shapes, not the same explicit function as usual, are also plotted. We only concern with dynamic analysis in frequency domain. In light of the exact dynamic solutions, the dynamic behavior in time domain can also be investigated.

Because of the complexity of the exact dynamic solutions for the PZT based smart structures, approximate solution procedures have been developed by various authors, e.g., Crawley and de Luis (1987), Crawley and Anderson (1990), Im and Atluri (1989), Shi and Atluri (1990), Gibbs and Fuller (1992), Rizet et al. (2000) and Tylikowski (2001). Based on the equivalent forces derived in the static analysis (Luo and Tong, 2002a,b), simple approximate solution procedures are presented and compared numerically with the exact dynamic solutions.

To further demonstrate the application and limitations of the approximate dynamic solutions, we also compare the exact dynamic solutions of the SLRM formulated in Part I (Tong and Luo, 2003) of this work

(see Appendix A of Part I) with the approximate solutions based on SLRM for two cases, namely, the host beam with one bonded PZT patch and the host beam with two symmetrically bonded PZT patches shown in Figs. 1 and 2. Useful conclusions are drawn from analyzing numerical results of the approximate and exact solutions based on the PSM and SLRM models.

2. Numerical results of a piezoelectric smart beam including peel stresses

2.1. A PZT used as an actuator

Based on the analytical solutions of steady state motions, the actuated dynamic performance can be investigated by letting the applied forces F and P be zero. In the subsequent analysis, it is assumed that a voltage of $V(=-100\sin\omega t\ v)$ is applied to the PZT patch.

2.1.1. Frequency spectrum in terms of the displacements at the free end

For the smart beam shown in Fig. 1, when the length of the host beam is chosen to be 0.2 m, displacements at the free end of the host beam can be calculated using the exact dynamic solutions for each given frequency of the applied voltage, whose results are plotted in Figs. 3 and 4. When the excitation frequency approaches to the resonant frequency, both the axial extension and lateral deflection become unlimited, leading to divergent solutions, and thus natural frequencies of the structure can be found. Figs. 3 and 4 give the frequency spectra in terms of the non-dimensional tip axial extension and lateral deflection.

2.1.2. Natural frequency and validation using the multi-segment shooting method

According to the frequency spectra shown in Figs. 3 and 4, the structural natural frequencies can be evaluated. The first eight orders of natural frequencies are listed in Table 1, in which, the results obtained by using the multi-segment shooting method (Tong et al., 2001; Sun et al., 2001) are also given for the purpose of comparison and verification. When the host beam length is chosen to be 0.6 m, relative differences of the eight natural frequencies between the exact solution and the results obtained by using the shooting method are all less than 0.1%. When the host beam length is 0.2 m, the eight natural frequencies predicted by the shooting method are 1% higher than those of the exact solutions. The examples demonstrate that the exact solutions are capable of reliably predicting natural frequencies.

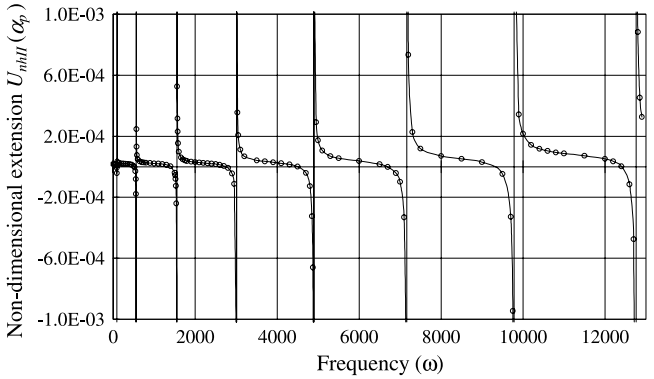

Fig. 3. Frequency spectra in terms of non-dimensional tip extension.

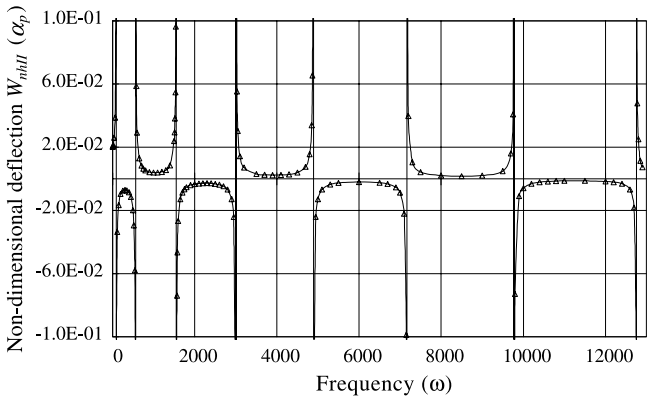

Fig. 4. Frequency spectra in terms of non-dimensional tip deflection.

Table 1
Natural frequencies and comparisons with the shooting method

Order	Natural frequency ω_n				Differences (%)	
	Exact solution		Shooting method			
	$L = 0.2$ m	$L = 0.6$ m	$L = 0.2$ m	$L = 0.6$ m	$L = 0.2$ m	$L = 0.6$ m
1	90.252	8.936	90.436	8.941	0.2038	0.0577
2	560.264	55.988	561.650	55.988	0.2468	0.0640
3	1553.061	156.646	1557.475	156.646	0.2834	0.0670
4	3005.712	306.705	3015.392	306.705	0.3210	0.0699
5	4891.526	506.555	4909.162	506.555	0.3592	0.0719
6	7164.347	755.992	7191.791	755.992	0.3816	0.0735
7	9782.129	1054.827	9815.772	1054.827	0.3427	0.0741
8	12,758.115	1402.852	12,784.638	1402.852	0.2075	0.0748

2.1.3. Steady state motions and normal mode shapes

The structural motions in steady state were given in Eqs. (32), (34) and (38) of Part I (Tong and Luo, 2003). When subjected to the excitations of an applied voltage with frequency ω, the displacement, velocity and acceleration at any point of the structure can be found. When the excitation frequency is equal to a natural frequency, the displacement will become infinite as no damping is considered in the analysis. The normal mode shape, approaching to the corresponding characteristic function, can be plotted by setting the value of the excitation frequency very close to the natural frequency. The normal mode shapes of the first eight orders are plotted in Figs. 5 and 6. The excitation frequencies indicated in both figures are 1.1634%, 0.2070%, 0.0805%, 0.0446%, 0.0288%, 0.0198%, 0.0133% and 0.0082% lower than the corresponding natural frequencies respectively.

The normal mode shapes shown in Figs. 5 and 6 are similar to those of a stepped cantilever beam with two different cross sections except for the portion where the PZT patch is bonded. However, the wavelength of each mode is shorter than that of the stepped beam as natural frequencies of the smart beam are higher than those of the stepped beam. For example, the first four order natural frequencies of the stepped beam are 76.02, 476.51, 1336.20 and 2627.55 (1/s), and they are 76.02, 476.38, 1333.88 and 2613.87 (1/s) for the uniform beam with the same cross section; relative differences of the natural frequency between the stepped beam and the uniform beam are less than 1%. However, the natural frequencies of the smart beams are 15.77%, 14.97%, 14.11% and 13.04% higher than those of the uniform beam respectively. It can be inferred

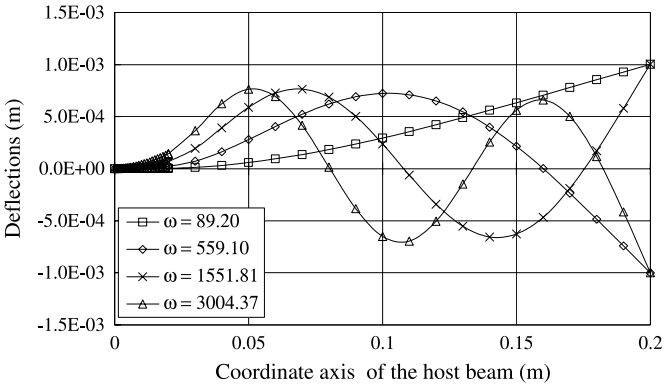

Fig. 5. Normal model shapes of orders 1 to 4.

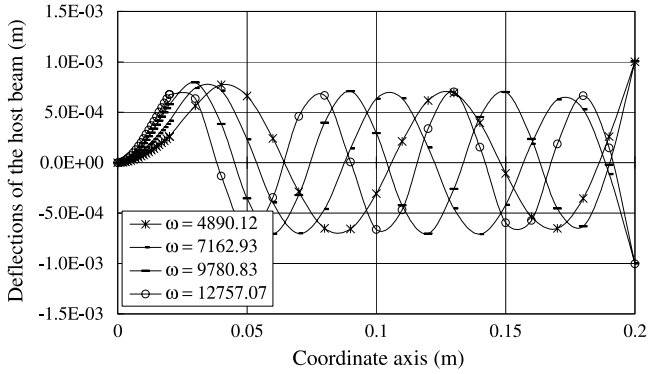

Fig. 6. Normal mode shapes of orders 5 to 8.

that the bonded PZT patch affects dynamics of smart beams due to its extra constraints rather than its geometry and mass.

Figs. 7 and 8 show the host beam extension excited by the same voltage as those used in Figs. 5 and 6. The extensional deformations are similar to those of the uniform stepped beam when the excitation frequency is lower. However, when the excitation frequency becomes higher, e.g., higher than the seventh natural frequency, coupling of the longitudinal and flexural vibrations becomes significant, and hence extensions of the smart beam are different from those of the stepped beam. In this case, the harmonic responses of the shear stress distributions are also different from those of the lower frequencies or in static state as will be discussed in the next section.

2.1.4. Harmonic responses on the actuated shear and peel stresses

The shear and peel stress distributions in static state were discussed in the exact static solutions (Luo and Tong, 2002b). The harmonic responses of the shear and peel stress distributions are shown in Figs. 9–12. Figs. 9 and 10 demonstrate distributions of the dynamic shear stresses. When the excitation frequency is lower, distributions of the dynamic shear stresses are similar to those in static state. In the present example, distribution patterns of the dynamic shear stresses are similar to those of the static shear stresses when the excitation frequency is lower than the fifth order natural frequency. However, when the excitation

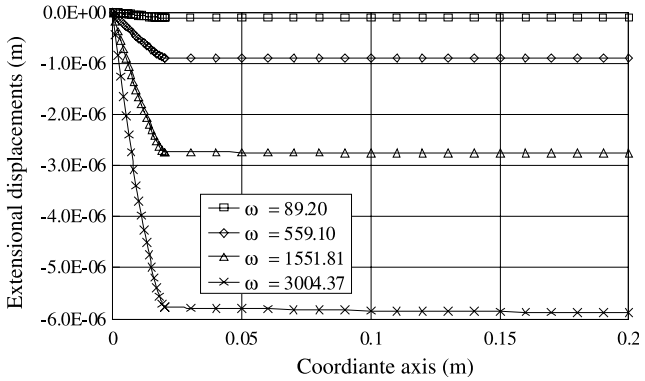

Fig. 7. Extensional responses related to normal modes of orders 1 to 4.

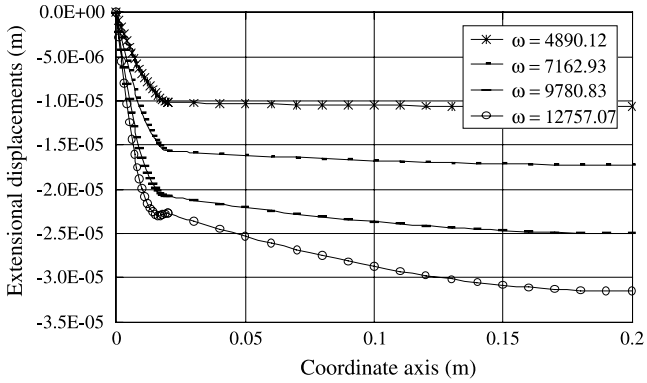

Fig. 8. Extensional responses related to normal modes of orders 5 to 8.

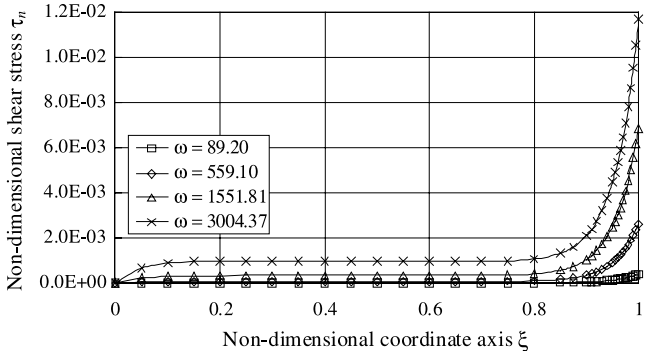

Fig. 9. Harmonic responses of shear stress distributions to lower frequencies.

frequency is higher than the fifth order natural frequency, the dynamic shear stress distributions, as clearly shown in Fig. 10, are different from those in static state.

Figs. 11 and 12 indicate that the distribution patterns of the dynamic peel stresses are the same as those of the static peel stresses, namely, peel stresses are highly concentrated near the free end and are almost zero

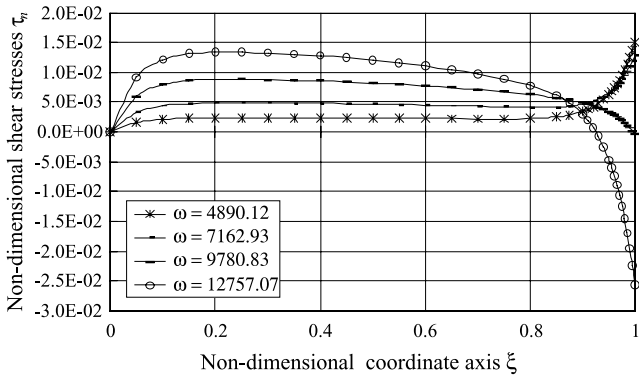

Fig. 10. Harmonic responses of shear stress distributions to relative high frequencies.

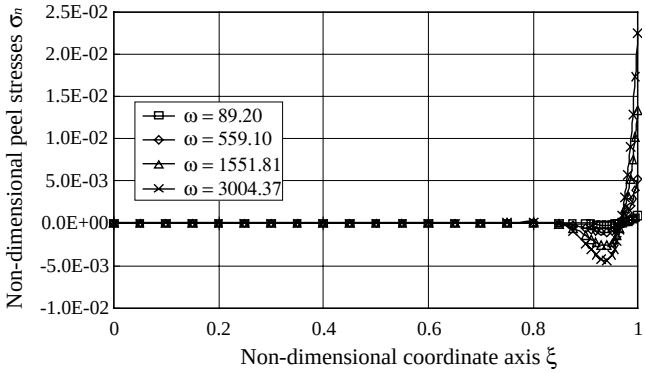

Fig. 11. Harmonic responses of peel stress distributions to lower frequencies.

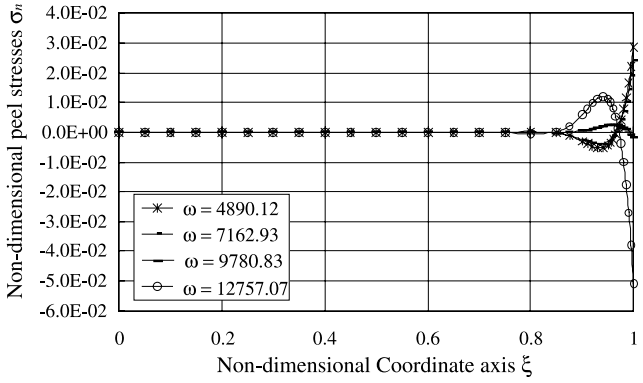

Fig. 12. Harmonic responses of peel stress distributions to relative high frequencies.

in the remaining area. The peek values of the peel stresses occur at the PZT edge in all cases, and thus only peel stresses near the free end area need to be considered.

Table 2
Comparisons of non-dimensional shear and peel stresses at the free PZT edge

Frequency, ω	Shear stress, τ_n	Peel stress, σ_n	Frequency, ω	Shear stress, τ_n	Peel stress, σ_n
1	−6.72E−05	2.65E−09	450	−5.66E−05	2.03E−05
10	−6.70E−05	2.68E−07	500	−3.26E−05	6.66E−05
20	−6.66E−05	1.11E−06	520	−6.47E−06	1.17E−04
40	−6.45E−05	5.24E−06	540	7.10E−05	2.66E−04
60	−5.85E−05	1.68E−05	550	2.23E−04	5.59E−04
80	−2.73E−05	7.71E−05	570	−4.08E−04	−6.58E−04
85	1.80E−05	1.65E−04	580	−2.44E−04	−3.41E−04
100	−1.25E−04	−1.12E−04	600	−1.64E−04	−1.86E−04
120	−9.14E−05	−4.69E−05	650	−1.19E−04	−9.98E−05
150	−8.31E−05	−3.08E−05	700	−1.06E−04	−7.46E−05
200	−7.89E−05	−2.26E−05	750	−9.93E−05	−6.19E−05
250	−7.64E−05	−1.79E−05	800	−9.51E−05	−5.39E−05
300	−7.40E−05	−1.31E−05	900	−8.94E−05	−4.30E−05
350	−7.08E−05	−6.96E−06	1000	−8.48E−05	−3.41E−05
400	−6.58E−05	2.57E−06	1100	−7.98E−05	−2.45E−05

In static state, the actuated peel stress is equal to zero for the smart beam shown in Fig. 1. As compared with the shear stresses, the peel stresses are small when the frequencies of an applied voltage are very low. Nevertheless, the peel stresses become larger with increase of frequencies. Table 2 compares the non-dimensional peak shear and peel stresses at the free end of the PZT for a frequency range of 1–1100 (1/s). When the frequency of applied voltage is equal to 1, 10 and 20 (1/s), the non-dimensional peak peel stress is 4, 2 and 1 order lower than the non-dimensional peak shear stress respectively. When the frequency is larger than 60 (1/s), the non-dimensional peak peel stress becomes in the same order as or significantly larger than the non-dimensional peak shear stress.

Moreover, Figs. 11 and 12 indicate that the peak peel stress induced at a higher natural frequency is significantly larger than that of the first order natural frequency. For the demonstrated example, the non-dimensional peak peel stress corresponding to the second to fifth order modes is 5.89, 15.1, 25.6 and 32.7 times of that of the first mode. Corresponding to the first to fifth modes, the peak peel stress is 127%, 97.6%, 94.1%, 92.6% and 91% higher than the peak shear stress respectively (see Figs. 9–12), and absolute values of the tip deflection all are 1 mm (see Figs. 5 and 6); therefore, the dynamic peel stress may cause edge debondings of the PZT patch.

In the static analysis (Luo and Tong, 2002a,b), we demonstrated that performance of the PZT actuators and sensors scarcely rely on the adhesive thickness when it is sufficiently thin. It can be shown that each order of natural frequency hardly depends on the adhesive thickness when it is very thin.

2.2. A PZT used as a sensor

Based on the analytical solutions given in Eqs. (32), (34) and (38), and the definitions of sensing charges (Lee, 1992), we can find the sensing charge caused by the applied force $F = F_0 \sin \omega t$ and $P = P_0 \sin \omega t$. Frequency spectra of the sensing charges are shown in Figs. 13 and 14, in which it is assumed that: $F_0 = 7.43 \times 10^{-6} \times E_h h$, and $P_0 = 7.43 \times E_h h^3/12$.

The natural frequencies can also be found from Fig. 13 or 14, and the results are the same as those determined from Fig. 3 or 4. The dynamic distribution patterns and the harmonic responses of the shear and peel stresses caused by the applied forces in the adhesive are the same as those induced by the applied voltage, and thus are not discussed in details here.

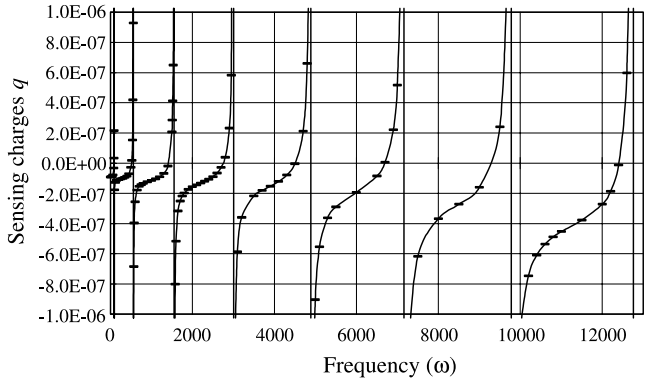

Fig. 13. Sensing charge q caused by an axial force vs. frequency ω.

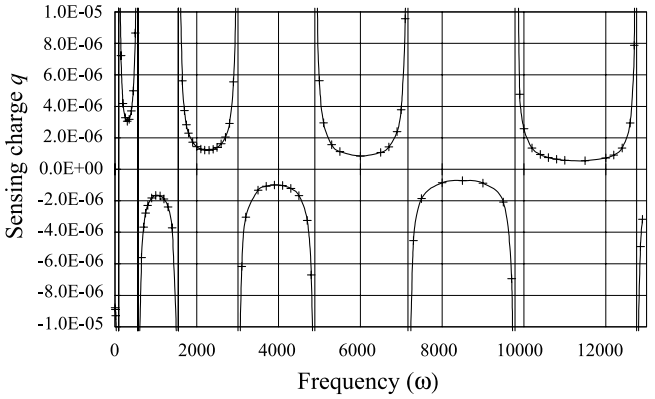

Fig. 14. Sensing charge q caused by a transverse force vs. frequency ω.

3. Comparisons with the shear lag models

In Part I of this work (Tong and Luo, 2003), exact dynamic solutions were derived for the shear lag beam model (SLBM) and the SLRM. To investigate effects of peel stresses on dynamic responses, we mainly compare PSM with SLBM, as the flexural motion of the PZT patch is not considered in SLRM.

3.1. Comparisons of frequency spectra with the shear lag beam model

Figs. 15 and 16 depict the frequency spectra predicted by using the PSM and SLBM models in terms of the non-dimensional tip deflection. In Figs. 15 and 16, the host beam length is chosen to be 0.2 m, and $L = 0.6$ m respectively. It is clear that, the natural frequencies predicted by SLBM are less than those of PSM. The dynamic peel strains in SLBM are shown in Eq. (67) in Part I (Tong and Luo, 2003). The energy transfer peel stresses are not included in SLBM, and thus it yields the lower natural frequency. The frequency spectra in Figs. 15 and 16 also indicate that SLBM underestimates the energy transfer between the PZT and the host structure. It is noted that, the shorter the host beam or the longer the PZT patch, the less the underestimations.

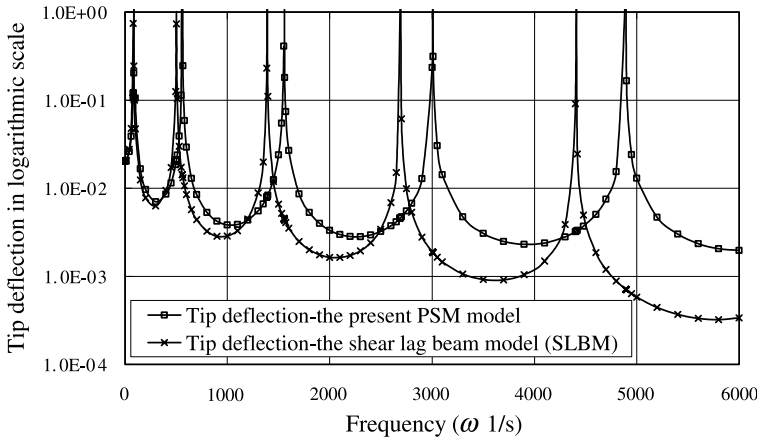

Fig. 15. Frequency spectra in terms of the non-dimensional tip deflection and comparison between the PSM and SLBM models for $L = 0.2$ m.

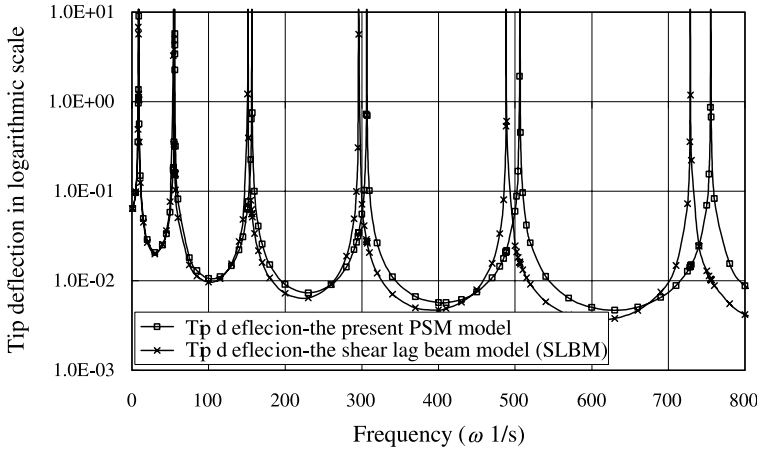

Fig. 16. Frequency spectra in terms of the non-dimensional tip deflection and comparison between the PSM and SLBM models for $L = 0.6$ m.

3.2. Comparisons of natural frequencies with the shear lag beam and rod models

Referring to the frequency spectra of Figs. 15 and 16, we can find the natural frequencies predicted by the PSM and SLBM models. The frequency spectra calculated using the SLRM model, not given here due to the space limitation, can also be plotted, from which the corresponding natural frequencies are found. It should be pointed out that, only the first five order and six order natural frequencies are shown in Figs. 15 and 16 respectively for clear presentation. Detailed comparisons of the first eight orders of natural frequencies are listed in Tables 3 and 4.

Table 3 presents the natural frequency comparisons for the host beam with a length of 0.2 m, and Table 4 for the host beam with a length of 0.6 m. In Tables 3 and 4, Error (b) and Error (r) columns refer to the errors of natural frequencies predicted by SLBM and SLRM as compared to those of the PSM. It can be seen that, the natural frequencies predicted by PSM are larger than those predicted by both SLBM and SLRM models,

Table 3
Comparisons of the natural frequencies for the host beam length of 0.2 m

Order	Natural frequencies, ω (1/s)			Error (b)	Error (r)
	PSM	SLBM	SLRM		
1	90.25	81.26	84.84	9.96	5.99
2	560.26	501.84	522.81	10.43	6.68
3	1553.06	1388.24	1441.73	10.61	7.17
4	3005.71	2690.24	2783.33	10.50	7.40
5	4891.53	4404.26	4542.43	9.96	7.14
6	7164.35	6519.40	6723.01	9.00	6.16
7	9782.13	8975.60	9341.97	8.24	4.50
8	12,758.12	11,227.30	12,418.01	12.00	2.67

Table 4
Comparisons of the natural frequencies for the host beam length of 0.6 m

Order	Natural frequencies			Error (b)	Error (r)
	PSM	SLBM	SLRM		
1	8.94	8.65	8.77	3.24	1.90
2	55.95	54.09	54.84	3.32	1.98
3	156.54	151.24	153.35	3.39	2.04
4	306.45	295.95	300.02	3.43	2.10
5	506.19	488.53	495.15	3.49	2.18
6	755.44	728.77	738.45	3.53	2.25
7	1054.05	1016.49	1029.68	3.56	2.31
8	1401.81	1351.54	1368.60	3.59	2.37

and the natural frequencies predicted by SLRM are larger than those by SLBM. When the host beam length is 0.2 m, the errors of the natural frequency predicted by SLBM are about 10%, and the errors of SLRM are less than 8%. When host beam length is 0.6 m, errors of the natural frequencies predicted by SLBM are in a range of 3–4%, and those of SLRM are about 2%.

Comparing the natural frequencies predicted by the PSM model and the SLBM/SLRM models, we can conclude that the peel strains in the adhesive layer provide the smart structure with extra constraints, and therefore both shear lag models give lower natural frequencies.

The reasons why the natural frequencies predicted by SLRM are larger than those by SLBM can be explained as: (a) the flexural motion of the PZT patch is not modeled in SLRM, and thus the structural stiffness increases, which leads to higher natural frequencies; (b) as the PZT mass is ignored for the structural flexural motion in SLRM, a decrease in structural mass also leads an increase in natural frequencies.

3.3. Dynamic responses of the shear stresses predicted by the shear lag model

3.3.1. Shear stresses of the shear lag beam model

Shear stresses defined in Eqs. (9) and (10) in Part I (Tong and Luo, 2003) of this work are the same as the shear stress expressions of SLBM, but the dynamic displacements of PSM are different from those of SLBM. When the structure is in static state, the boundary conditions of the smart beam shown in Fig. 1 for PSM are the same as those for SLBM. Hence, the statically actuated shear stresses of the smart beam in Fig. 1 predicted by SLBM are the same as those of PSM. When the excitation frequency of the applied voltage is low, the shear stresses predicted by both models are also the same, e.g., when the excitation

frequency is less than 10 (1/s), the difference of peak shear stress predicted by SLBM and PSM is less than 0.001%. When the excitation frequency is 40 and 60 (1/s), the peak value of the non-dimensional shear stress predicted by SLBM is -6.45×10^{-5} and -5.85×10^{-5}, whose absolute value is 0.262% and 3.57% higher than that of PSM respectively. The distribution patterns of shear stresses for both models are the same. However, when the excitation frequency becomes high, the difference of shear stresses between SLBM and PSM can be very large, and it becomes too large to conduct a comparison when the excitation frequency is close to a resonant frequency. It is worthwhile noting that, when the adherends of smart beams are not identical, shear stresses in static state predicted by PSM and SLBM are different.

3.3.2. Stress distributions in harmonic responses predicted by the shear lag beam model

When the excitation frequency is close to a resonant frequency, non-dimensional shear stress distributions in harmonic responses are shown in Figs. 17 and 18. Each curve in the figures represents an individual normal mode corresponding to a natural frequency between order 1 and order 8.

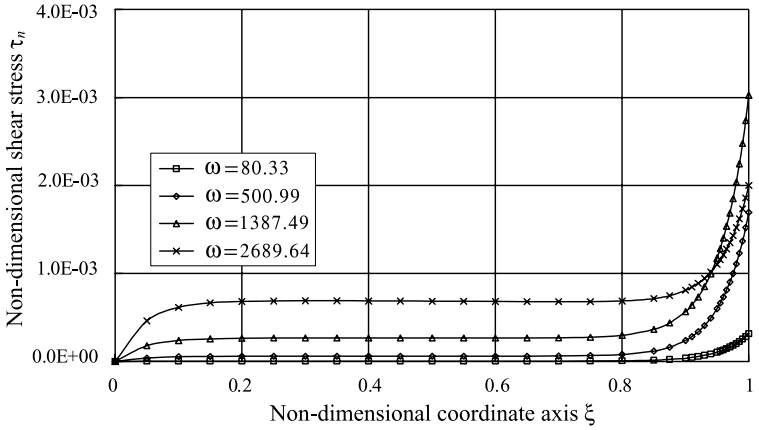

Fig. 17. Harmonic responses of shear stress distributions to lower frequencies predicted by the shear lag beam model when $L = 0.2$ m.

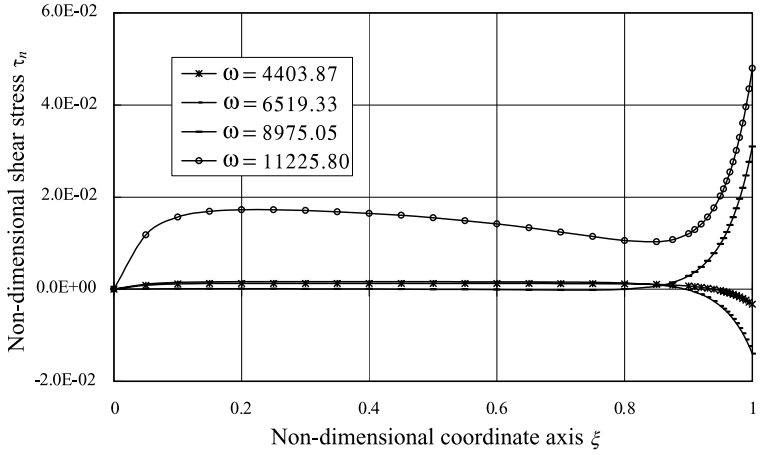

Fig. 18. Harmonic responses of shear stress distributions to higher frequencies predicted by the shear lag beam model when $L = 0.2$ m.

A comparison of the distributions of the dynamic shear stress of PSM shown in Figs. 9 and 10 reveals that the distribution patterns predicted by SLBM are similar to those of the static shear stress only for the first three vibration modes. When the excitation frequency is higher, the shear stresses may not peak near the PZT free edges. When the vibration mode is equal to the eighth order frequency, distributions of the shear stress predicted by SLBM is different from those of lower modes due to significant coupling between the extensional and flexural motions.

In static state, when two PZT edges are free, distributions of the actuated shear stresses come in an anti-symmetric form. Because of the existence of the inertial forces in dynamics, shear stresses no longer form anti-symmetrically, which can be readily understood by considering the dynamic equilibrium conditions of the PZT patch.

4. Approximate analysis of dynamics for a smart beam based on equivalent forces

Crawley and de Luis (1987) directly applied equivalent forces derived from their static analysis to dynamics. In their opinion, when PZT patches are significantly thinner than the host beam, the PZT mass and geometry could be ignored, and thus the applied voltages to the PZT patches only excite the host beam. Similarly, Gibbs and Fuller (1992) concluded that, a single actuator is mathematically equivalent to equal and opposite moments, and simultaneously equal and opposite in-plane forces located at both ends of the actuator.

We showed in the static analysis (Luo and Tong, 2002a,b) that, the actuated equivalent forces based on the shear lag models can lead to large errors in analyzing flexible structures; therefore, the equivalent force expressions derived in the static analysis are employed here. The PZT mass and geometry (0.5–2 mm thick) are included in the approximate solutions for investigating its effects on dynamics.

To obtain the reasonable and concise equations, we neglect the adhesive thickness (0.05–0.2 mm, Anderson et al., 1977; Tong and Steven, 1999) and mass in the following derivations.

4.1. Formulation of the approximate dynamic solutions based on equivalent force

In our analysis, the theoretical fundamentals are based on that, peel stresses are highly concentrated near the small free end areas and almost zero in the remaining areas. In majority of the PZT patch, $w_h - w_1 = 0$, or $w_h = w_1 = w_{p0}$, where w_{p0} is the flexural displacement of the neutral layer of a smart beam where the PZT patch is bonded. This is also the assumption in our derivation of the equivalent forces based on the equilibrium differential equations. The present equivalent forces correlate extremely well with the exact static solutions to PZT smart beams including peel stress (Luo and Tong, 2002a,b).

Although the dynamic solutions are derived only to the model in Fig. 1, the analytical procedure can be applied to other host beams with bonded one PZT patch or two PZT patches. It can also be extended to the smart beam with the distributed PZT patches.

Solutions to section I of the host beam can be given by

$$u_{nhI} = U_{nhI} \sin \Omega t_n, \qquad w_{nhI} = W_{nhI} \sin \Omega t_n \tag{1}$$

$$\left.\begin{aligned} U_{nhI} &= A_{p1} \sin \beta_{s1}\xi + A_{p2} \cos \beta_{s1}\xi \\ &\quad - \frac{r_h}{2}\beta_p[(B_{p1} \cosh \beta_p\xi + B_{p2} \sinh \beta_p\xi + B_{p3} \cos \beta_p\xi - B_{p4} \sin \beta_p\xi)] \\ W_{nhI} &= (B_{p1} \sinh \beta_p\xi + B_{p2} \cosh \beta_p\xi + B_{p3} \sin \beta_p\xi + B_{p4} \cos \beta_p\xi) \end{aligned}\right\} \tag{2}$$

where,

$$\beta_p = \sqrt{\frac{\omega}{\alpha_{wp}}}, \qquad \alpha_{wp} = \sqrt{\frac{E_{nh} r_h^4}{3 m_T}} \tag{3}$$

Solutions to section II of the host beam are

$$u_{nhII} = U_{nhII} \sin \Omega t_n, \qquad w_{nhII} = W_{nhII} \sin \Omega t_n \tag{4}$$

$$\left.\begin{aligned} U_{nhII} &= A_{h1} \sin \beta_{s1}\xi + A_{h2} \cos \beta_{s1}\xi \\ W_{nhII} &= B_{h1} \sinh \beta_h \xi + B_{h2} \cosh \beta_h \xi + B_{h3} \sin \beta_h \xi + B_{h4} \cos \beta_h \xi \end{aligned}\right\} \tag{5}$$

When only the actuated performance are considered, the boundary conditions are
Section I of the host beam:

$$\left.\begin{aligned} &\xi = 0 : U_{nhI} = 0 \quad \xi = 1 : \frac{\mathrm{d}U_{nhI}}{\mathrm{d}\xi} = (\varepsilon_N - \varepsilon_{eqdN}) \\ &W_{nhI} = 0 \qquad\qquad \frac{\mathrm{d}^2 W_{nhI}}{\mathrm{d}\xi^2} = -(\varepsilon_M - \varepsilon_{eqdM}) \\ &\frac{\mathrm{d}W_{nhI}}{\mathrm{d}\xi} = 0 \qquad\qquad \frac{\mathrm{d}^3 W_{nhI}}{\mathrm{d}\xi^3} = -\varepsilon_Q \end{aligned}\right\} \tag{6}$$

where,

$$\varepsilon_{eqdN} = \frac{N_{eqdN}}{E_{nh} r_h}, \qquad \varepsilon_{eqdM} = \frac{12 M_{eqdM}}{E_{nh} r_h^3} \tag{7}$$

In Eq. (7), N_{eqdN} and M_{eqdM} are the equivalent actuated forces given in the exact static solutions (Luo and Tong, 2002a,b). It should be noted that the definitions of non-dimensional parameters are different.
Section II of the host beam:

$$\left.\begin{aligned} &\xi = 0 : \frac{\mathrm{d}U_{nhII}}{\mathrm{d}\xi} = \varepsilon_N, \quad \xi = \alpha_p = \frac{L - L_p}{L_p} : \frac{\mathrm{d}U_{nhII}}{\mathrm{d}\xi} = 0 \\ &\frac{\mathrm{d}^2 W_{nhII}}{\mathrm{d}\xi^2} = -\varepsilon_M, \qquad \frac{\mathrm{d}^2 W_{nhII}}{\mathrm{d}\xi^2} = 0 \\ &\frac{\mathrm{d}^3 W_{nhII}}{\mathrm{d}\xi^3} = -\varepsilon_Q, \qquad \frac{\mathrm{d}^3 W_{nhII}}{\mathrm{d}\xi^3} = 0 \end{aligned}\right\} \tag{8}$$

Substituting the boundary conditions at $\xi = 0$ into the motion equation of section I, we have

$$\left.\begin{aligned} U_{nhI} &= A_{p1} \sin \beta_{s1}\xi - \tfrac{r_h}{2} \beta_p [B_{p1}(\cosh \beta_p \xi - \cos \beta_p \xi) + B_{p2}(\sinh \beta_p \xi + \sin \beta_p \xi)] \\ W_{nhI} &= B_{p1}(\sinh \beta_p \xi - \sin \beta_p \xi) + B_{p2}(\cosh \beta_p \xi - \cos \beta_p \xi) \end{aligned}\right\} \tag{9}$$

Substituting the boundary conditions at $\xi = 1$ into the motion equation of section I, we obtain:

$$A_{p1} \beta_{s1} \cos \beta_{s1} - \frac{r_h}{2} \beta_p^2 [B_{p1}(\sinh \beta_p + \sin \beta_p) + B_{p2}(\cosh \beta_p + \cos \beta_p)] = (\varepsilon_N - \varepsilon_{eqdN}) \tag{10}$$

$$\left.\begin{aligned} &B_{p1}(\sinh \beta_p + \sin \beta_p) + B_{p2}(\cosh \beta_p + \cos \beta_p) = -\frac{1}{\beta_p^2}(\varepsilon_M - \varepsilon_{eqdM}) \\ &B_{p1}(\cosh \beta_p + \cos \beta_p) + B_{p2}(\sinh \beta_p - \sin \beta_p) = -\frac{1}{\beta_p^3}\varepsilon_Q \end{aligned}\right\} \tag{11}$$

Integration constants A_{p1}, B_{p1} and B_{p2} are solved from Eqs. (10) and (11):

$$A_{p1} = \frac{(\varepsilon_N - \varepsilon_{eqdN}) - \frac{r_h}{2}(\varepsilon_M - \varepsilon_{eqdM})}{\beta_{s1}\cos\beta_{s1}} \tag{12}$$

$$B_{p1} = \frac{\Delta_{p1}}{\Delta_p}, \qquad B_{p2} = \frac{\Delta_{p2}}{\Delta_p} \tag{13}$$

$$\left.\begin{aligned} \Delta_p &= 2(\cosh\beta_p\cos\beta_p + 1) \\ \Delta_{p1} &= \frac{1}{\beta_p^3}[(\varepsilon_M - \varepsilon_{eqdM})\beta_p(\sinh\beta_p - \sin\beta_p) - \varepsilon_Q(\cosh\beta_p + \cos\beta_p)] \\ \Delta_{p2} &= \frac{1}{\beta_p^3}[-(\varepsilon_M - \varepsilon_{eqdM})\beta_p(\cosh\beta_p + \cos\beta_p) + \varepsilon_Q(\sinh\beta_p + \sin\beta_p)] \end{aligned}\right\} \tag{14}$$

Substituting the boundary conditions at $\xi = 0$ and $\xi = \alpha_p$ into the motion equations of section II, we can solve:

$$\left.\begin{aligned} U_{nhII} &= \frac{1}{\beta_{s1}\sin\beta_{s1}\alpha_p}\cos\beta_{s1}(\alpha_p - \xi)\varepsilon_N \\ W_{nhII} &= \frac{\Delta_{h1}}{\Delta_h}(\sinh\beta_h\xi + \sin\beta_h\xi) + \frac{\Delta_{h2}}{\Delta_h}(\cosh\beta_h\xi + \cos\beta_h\xi) + \frac{\cos\beta_h\xi}{\beta_h^2}\varepsilon_M + \frac{\sin\beta_h\xi}{\beta_h^3}\varepsilon_Q \end{aligned}\right\} \tag{15}$$

where,

$$\left.\begin{aligned} \Delta_h &= 2(\cosh\beta_h\alpha_p\cos\beta_h\alpha_p - 1) \\ \Delta_{h1} &= \frac{1}{\beta_h^3}[\beta_h(\sinh\beta_h\alpha_p\cos\beta_h\alpha_p + \cosh\beta_h\alpha_p\sin\beta_h\alpha_p)\varepsilon_M \\ &\quad +(\sinh\beta_h\alpha_p\sin\beta_h\alpha_p - \cosh\beta_h\alpha_p\cos\beta_h\alpha_p + 1)\varepsilon_Q] \\ \Delta_{h2} &= \frac{1}{\beta_h^3}[-\beta_h(\sinh\beta_h\alpha_p\sin\beta_h\alpha_p + \cosh\beta_h\alpha_p\cos\beta_h\alpha_p - 1)\varepsilon_M \\ &\quad +(\sinh\beta_h\alpha_p\cos\beta_h\alpha_p - \cosh\beta_h\alpha_p\sin\beta_h\alpha_p)\varepsilon_Q] \end{aligned}\right\} \tag{16}$$

In Eqs. (9) and (15), the unknown intersectional forces between sections I and II can be solved by the continuity and smooth conditions of the host beam:

$$U_{nhI}(1) = U_{nhII}(0), \quad W_{nhI}(1) = W_{nhII}(0), \quad \frac{\mathrm{d}W_{nhI}(1)}{\mathrm{d}\xi} = \frac{\mathrm{d}W_{nhII}(0)}{\mathrm{d}\xi} \tag{17}$$

Utilizing Eqs. (9), (15) and (17), the intersectional forces can be solved by

$$\left.\begin{aligned} P_{11}\varepsilon_M + P_{12}\varepsilon_Q &= c_{1M}\varepsilon_{eqdM} \\ P_{21}\varepsilon_M + P_{22}\varepsilon_Q &= c_{2M}\varepsilon_{eqdM} \end{aligned}\right\} \tag{18}$$

$$P_{01}\varepsilon_N + P_{02}\varepsilon_M + P_{03}\varepsilon_Q = c_{0N}\varepsilon_{eqdN} + c_{0M}\varepsilon_{eqdM} \tag{19}$$

where,

$$\left.\begin{aligned} P_{11} &= -\frac{\sinh\beta_p\sin\beta_p}{\beta_p^2(\cosh\beta_p\cos\beta_p + 1)} + \frac{\sinh\beta_h\alpha_p\sin\beta_h\alpha_p}{\beta_h^2(\cosh\beta_h\alpha_p\cos\beta_h\alpha_p - 1)} \\ P_{12} &= -\frac{\sinh\beta_p\cos\beta_p - \cosh\beta_p\sin\beta_p}{\beta_p^3(\cosh\beta_p\cos\beta_p + 1)} - \frac{\sinh\beta_h\alpha_p\cos\beta_h\alpha_p - \cosh\beta_h\alpha_p\sin\beta_h\alpha_p}{\beta_h^3(\cosh\beta_h\alpha_p\cos\beta_h\alpha_p - 1)} \end{aligned}\right\} \tag{20}$$

$$\left.\begin{aligned} P_{21} &= -\frac{\sinh\beta_p\cos\beta_p+\cosh\beta_p\sin\beta_p}{\beta_p(\cosh\beta_p\cos\beta_p+1)}-\frac{\sinh\beta_h\alpha_p\cos\beta_h\alpha_p+\cosh\beta_h\alpha_p\sin\beta_h\alpha_p}{\beta_h(\cosh\beta_h\alpha_p\cos\beta_h\alpha_p-1)} \\ P_{22} &= \frac{\sinh\beta_p\sin\beta_p}{\beta_p^2(\cosh\beta_p\cos\beta_p+1)}-\frac{\sinh\beta_h\alpha_p\sin\beta_h\alpha_p}{\beta_h^2(\cosh\beta_h\alpha_p\cos\beta_h\alpha_p-1)} \end{aligned}\right\} \tag{21}$$

$$\left.\begin{aligned} P_{01} &= \frac{\tan\beta_{s1}}{\beta_{s1}}-\frac{\cos\beta_{s1}\alpha_p}{\beta_{s1}\sin\beta_{s1}\alpha_p} \\ P_{02} &= \frac{r_h}{2}\left[\frac{\sinh\beta_p\cos\beta_p+\cosh\beta_p\sin\beta_p}{\beta_p(\cosh\beta_p\cos\beta_p+1)}-\frac{\tan\beta_{s1}}{\beta_{s1}}\right] \\ P_{03} &= -\frac{r_h}{2}\frac{\sinh\beta_p\sin\beta_p}{\beta_p^2(\cosh\beta_p\cos\beta_p+1)} \end{aligned}\right\} \tag{22}$$

$$\left.\begin{aligned} c_{0N} &= \frac{\tan\beta_{s1}}{\beta_{s1}}, \qquad c_{0M}=\frac{r_h}{2}\left[\frac{\sinh\beta_p\cos\beta_p+\cosh\beta_p\sin\beta_p}{\beta_p(\cosh\beta_p\cos\beta_p+1)}-\frac{\tan\beta_{s1}}{\beta_{s1}}\right] \\ c_{1M} &= -\frac{\sinh\beta_p\sin\beta_p}{\beta_p^2(\cosh\beta_p\cos\beta_p+1)} \\ c_{2M} &= -\frac{\sinh\beta_p\cos\beta_p+\cosh\beta_p\sin\beta_p}{\beta_p(\cosh\beta_p\cos\beta_p+1)} \end{aligned}\right\} \tag{23}$$

The steady motions of sections I and II are shown in Eqs. (9) and (15), in which, ε_N, ε_M and ε_Q are determined by Eqs. (18) and (19).

4.2. Numerical comparisons with the exact solutions

Fig. 19 gives comparisons of the frequency spectra between the approximate and exact dynamic solutions for PSM. It can be seen that the natural frequency of each order predicted by the approximate solutions are lower than that of the exact dynamic solutions, with an error of more than 10%. It should be

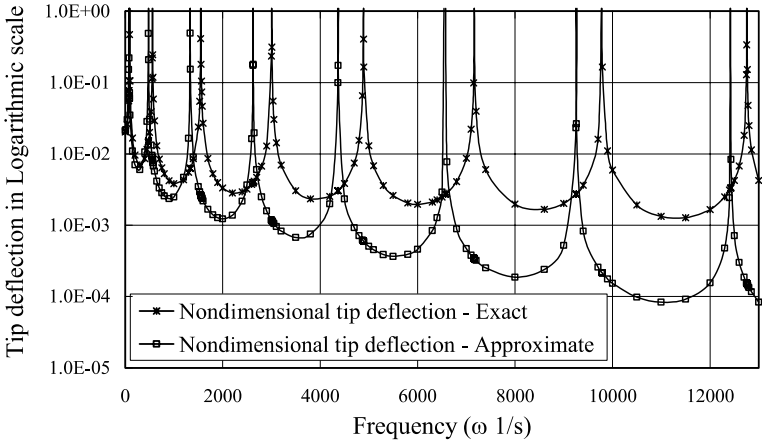

Fig. 19. Frequency spectra predicted by the approximate and exact solutions ($L = 0.2$ m).

noted that the mass and geometry have been considered in the approximate solutions. It can be shown that, the natural frequencies predicted by the present approximate solutions are only slightly higher than (less than 1%) those of the uniform cantilever beam with no bonded PZT patch for this case. Therefore, it is further confirmed that the bonded PZT patches affect dynamics of smart structures due to the extra constraints rather than the geometry and mass. Fig. 20 is another example of the frequency spectrum comparisons when the host beam length is 0.6 m, and the natural frequency differences are about 5%. It is evident that the approximate solutions yield a large error of the natural frequency and may not be directly used to represent a general dynamic analysis of flexible structures.

When the excitation frequency is very low, non-dimensional tip displacements are shown in Figs. 21 and 22. This case may be considered as the quasi-static state. Fig. 21 shows that, when $\omega < 30$ 1/s, the errors of the tip deflection predicted by the approximate solutions are less than 10%, which is mainly caused by use of

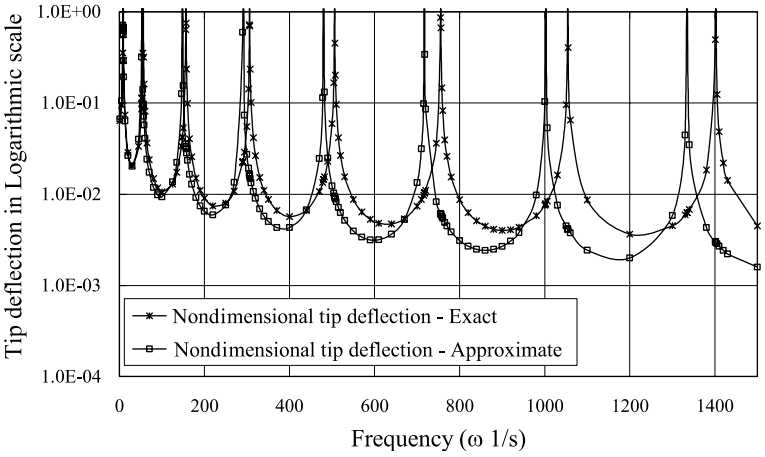

Fig. 20. Frequency spectra predicted by the approximate and exact solutions ($L = 0.6$ m).

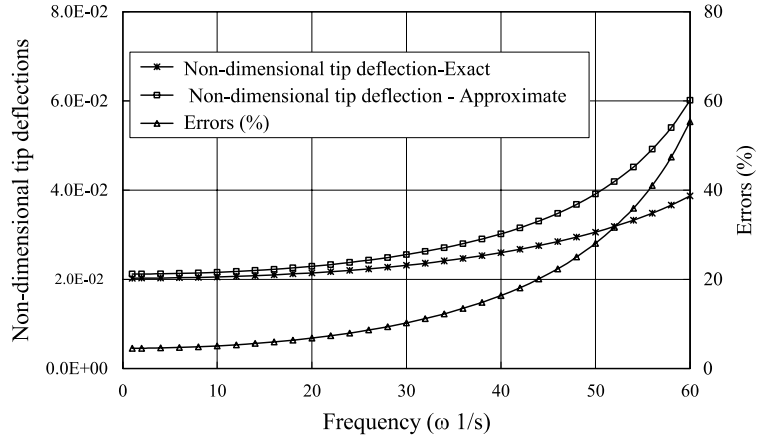

Fig. 21. Tip deflections predicted by the approximate and exact solutions ($L = 0.2$ m).

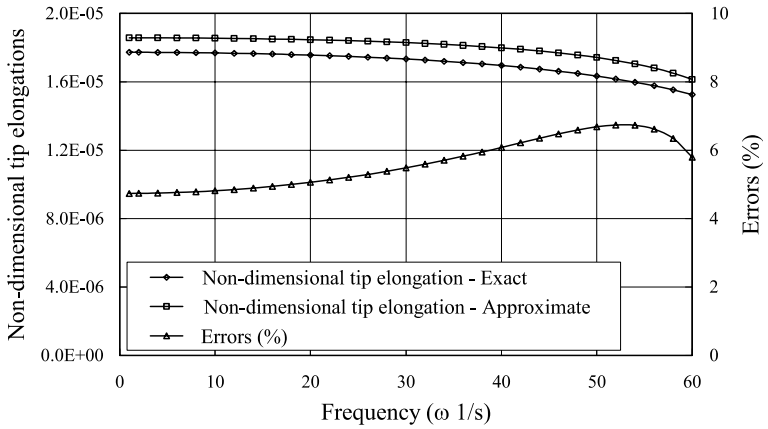

Fig. 22. Tip elongations predicted by the approximate and exact solutions ($L = 0.2$ m).

the static equivalent forces. When the excitation frequency becomes higher, the results of the approximate solution can be significantly different from those of the exact solutions. This indicates that the approximate solution may be only used in quasi-static state.

The comparison of the tip extension between the approximate and exact dynamic solutions is shown in Fig. 22. Fig. 22 reveals that, when the frequency is low (lower than the first natural frequency), the error of the approximate solutions for extension is in the range of 4–7%, which is also due to the error introduced in the static equivalent forces. Therefore, the approximate solutions only give the quasi-static results in analyzing the dynamic responses. In addition, the coupled flexural motion must be included in the extensional motion. Otherwise, the non-dimensional tip elongation predicted by the approximate solution is constant, leading to a large error within the excitation frequency range in Fig. 22.

Now we consider a case that the PZT patch in Fig. 1 is not fixed to the clamped end. Natural frequency predicted by the approximate solution is the same for the cases: (a) free two PZT ends, and (b) fixed one PZT end and free the other end. The two cases are also studied using the multi-segment shooting method. The results given in Table 5 were obtained using the method developed by one of the authors (Tong et al., 2001 and Sun et al., 2001). The comparison between the exact solutions given in Table 1 shows that there exists an excellent agreement between the exact solutions and the numerical method. Table 5 gives com-

Table 5
Comparisons of natural frequency for the free PZT ends and the fixed PZT one end

Order	Natural frequency ω_n				Differences (%)	
	(a) Free two PZT ends		(b) Fixed one PZT end and free the other end			
	$L = 0.2$ m	$L = 0.6$ m	$L = 0.2$ m	$L = 0.6$ m	$L = 0.2$ m	$L = 0.6$ m
1	89.510	8.916	90.436	8.941	1.0248	0.2797
2	552.689	55.803	561.650	55.988	1.5956	0.3307
3	1522.597	156.051	1557.475	156.646	2.2394	0.3798
4	2921.892	305.374	3015.392	306.705	3.1008	0.4339
5	4703.758	504.064	4909.162	506.555	4.1841	0.4917
6	6819.889	751.801	7191.791	755.992	5.1712	0.5544
7	9293.075	1048.267	9815.772	1054.827	5.3251	0.6219
8	12,220.220	1393.088	12,784.638	1402.852	4.4148	0.6960

parisons of natural frequency for the free PZT ends and the fixed PZT one end. When the host beam length is 0.6 m, the differences of the first eight order of natural frequency are all less than 1%. When the host beam length is 0.2 m, the differences of the first two order of natural frequency are less than 2%. The present results illustrate that, when the PZT edge is free from the clamped end, the natural frequencies only decrease slightly, and hence the extra constraints, leading to higher natural frequencies, are mainly caused by the PZT motions.

5. Application limitations of the approximate solutions

The previous section shows that the approximate dynamic solutions could estimate the dynamic responses only when the excited frequency is very low for flexible structures. When the host beam-to-PZT thickness ratio R_{ht} is very large, the approximate dynamic solution based on the static equivalent forces may be available in light of the work conducted by Crawley and de Luis (1987), Crawley and Anderson (1990), Im and Atluri (1989) and Shi and Atluri (1990). In this section, we will further investigate the limitations of the approximate dynamic solutions by comparing the exact and approximate solutions using the SLRM.

When PZT mass is ignored, the natural frequencies based on the approximate solution are the same as those of the uniform beam. The natural frequencies and the dynamic responses predicted by the exact and approximate solutions will be illustrated for smart beams shown in Figs. 1 and 2.

5.1. A cantilever beam with one bonded PZT patch

Figs. 23 and 24 plot the first three natural frequencies vs. thickness ratio R_{ht} predicted by the exact solutions of SLRM given in Appendix A of Part I (Tong and Luo, 2003) and approximate solutions for a cantilever beam with one bonded PZT patch when $L = 0.6$ m shown in Fig. 1. In both figures, the frequency is scaled by dividing the thickness ratio R_{ht} for clarity.

Fig. 23 gives the comparison of the first natural frequency. When the host beam-to-PZT thickness ratio R_{ht} is equal to 1, the difference between the exact and approximate solutions is 3.69%, and it is less than 1% when R_{ht} is larger than 15. The second and third natural frequencies predicted by the exact and approximate solutions of SLRM are shown in Fig. 24, whose differences have a pattern similar to that of the first natural

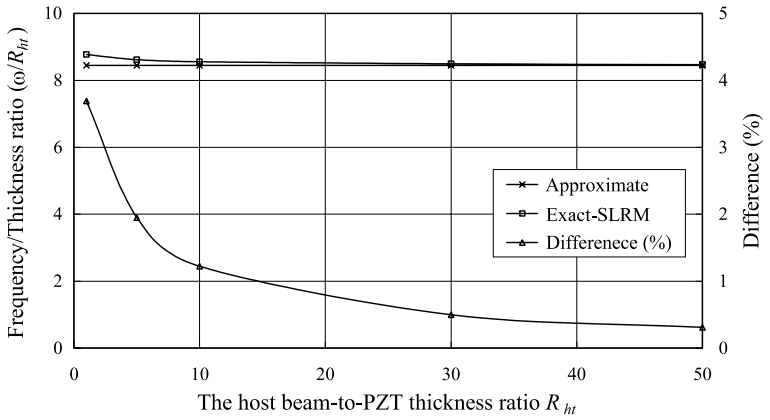

Fig. 23. The lowest natural frequency predicted by the exact and approximate solutions when $L = 0.6$ m.

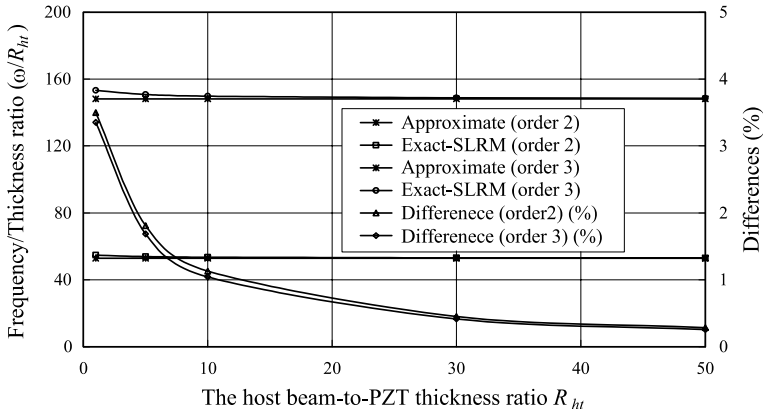

Fig. 24. The second and third natural frequencies predicted by the exact and approximate solutions when $L = 0.6$ m.

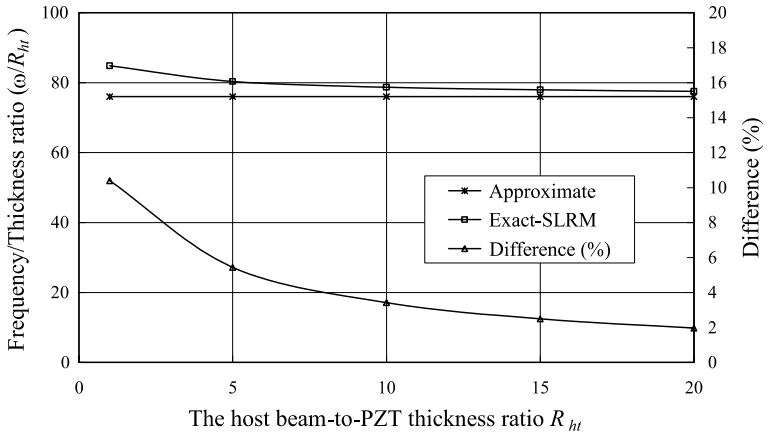

Fig. 25. The lowest natural frequencies predicted by the exact and approximate solutions when $L = 0.2$ m.

frequency. The differences of natural frequency predicted by the exact and approximate solutions slightly decrease for the second and third order frequencies.

The differences of natural frequency predicted by the exact and approximate solutions are not only related to the host beam-to-PZT thickness ratio, but they also depend on the host beam-to-PZT length ratio $R_{Lp}(= L/L_p)$. Fig. 25 compares the first order natural frequency predicted by the approximate and exact solutions of SLRM when L is 0.2 m or $R_{Lp} = 10$. It can be seen that, when the host beam-to-PZT thickness ratio R_{ht} is equal to 1, the difference between the exact and approximate solutions is 10.4%; it is 5.44%, 3.42%, 2.49% and 1.96% when $R_{ht} = 5$, 10, 15 and 20 respectively.

Only when the PZT patch is significantly thinner and shorter than the host beam, the approximate solutions possess the sufficient accuracy for natural frequency of smart beams. The natural frequency predicted by the present approximate solution appears to have little difference from those of the uniform beam for all of the above cases, even though it includes the PZT mass and geometric size. It can also be drawn that the bonded PZT patches with relative soft adhesive provide smart structures with extra constraints rather than the mass and geometric sizes.

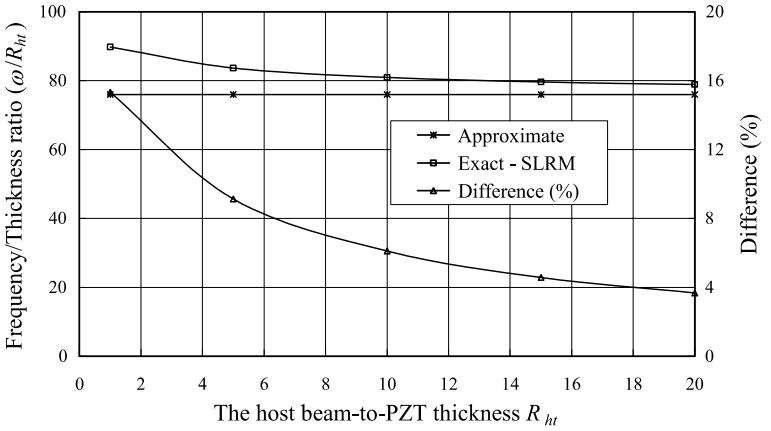

Fig. 26. The lowest natural frequencies predicted by the exact and approximate solutions for the host beam with two symmetrically bonded PZT patches when $L = 0.2$ m.

5.2. A cantilever beam with two symmetrically bonded PZT patches

When the host beam are symmetrically bonded with two bonded PZT patches as shown in Fig. 2, exact solutions of SLRM can be transferred to two cases, namely, extensional motion and flexural motion of the host beam, see Appendix A in Part I (Tong and Luo, 2003) of this work. Here, we present flexural motion only due to the space limitation. It is assumed that voltages of $V_{pa} = (V_1 - V_2)/2 = -100 \sin \omega t(v)$ are applied to the PZT patches.

Fig. 26 illustrates the natural frequency of the host beam with two symmetrically bonded PZT patches predicted by the approximate and exact solutions when $L = 0.2$ m. When the host beam-to-PZT thickness ratio R_{ht} is 1, 5, 10, 15 and 20, the lowest natural frequency predicted by the approximate solution is 15.33%, 9.14%, 6.10%, 4.58% and 3.67% lower than that predicted by the exact solution of SLRM respectively.

When the host beam length is 0.6 m, or a relatively short PZT patch is used, the lowest natural frequency predicted by the approximate solution is 5.31%, 3.23%, 2.18%, 0.94% and 0.61% lower than that of the exact solution of SLRM, when the host beam-to-PZT thickness ratio R_{ht} is chosen to be 1, 5, 10, 30 and 50.

It can be seen that the natural frequency of the host beam with two symmetrically bonded PZT patches is apparently higher than the host beam with one bonded PZT patch, which further indicates the extra constraints induced by the extra PZT patch motions.

When the length of the host beam with two bonded PZTs is 0.6 m and the thickness ratio R_{ht} is larger than 30, the errors of natural frequencies predicted by the approximate solution are less than 1%. However, the errors of dynamic responses predicted by the approximate solutions of SLRM are not as small as those of frequencies. When the host beam deforms in pure bending actuated by the applied voltages, the non-dimensional tip deflections for $R_{ht} = 30$ and 50 predicted by the approximate and exact solutions of SLRM are shown in Figs. 27 and 28. Although the errors of natural frequency predicted by the approximate solution are less than 1% for these cases, both non-dimensional tip deflections predicted by the approximate solution are about 13% higher than those of the exact solution when the excitation frequency is low, and the error increases with the excitation frequency. When the excitation frequency is close to the natural frequency, the error increases dramatically, which indicates that the approximate solution is not suitable in this case.

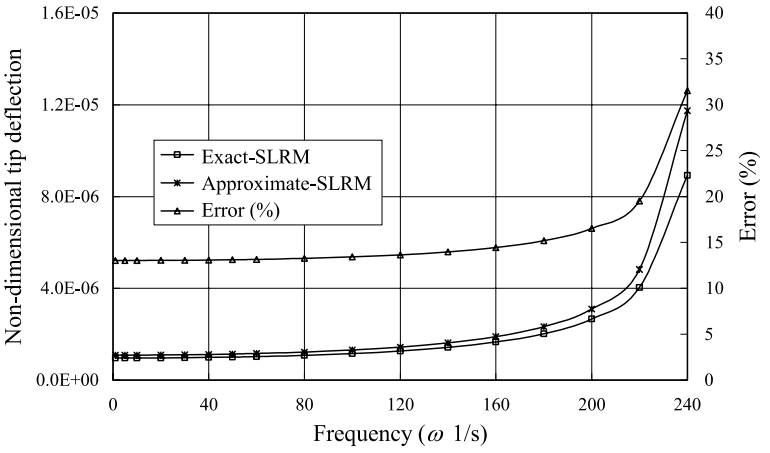

Fig. 27. Non-dimensional tip deflections predicted by the exact and approximate solutions when thickness ratio $R_{ht} = 30$ and length ratio $R_{Lp} = 30$.

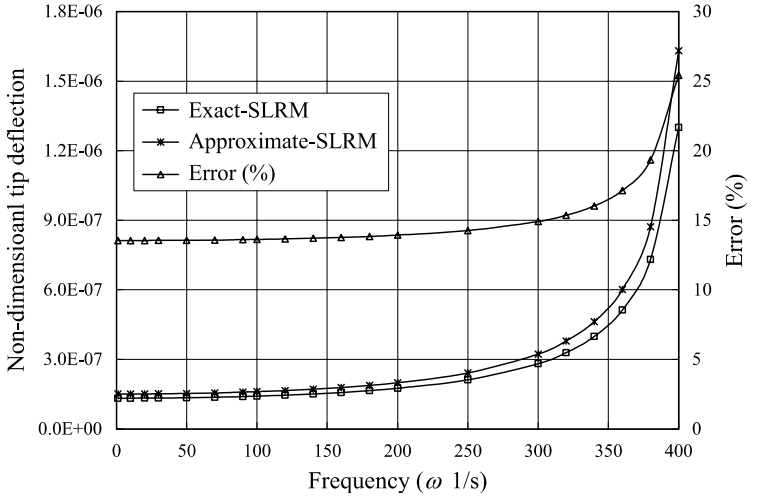

Fig. 28. Non-dimensional tip deflections predicted by the exact and approximate solutions when thickness ratio $R_{ht} = 50$ and length ratio $R_{Lp} = 30$.

6. Discussion

6.1. Effects of the shear and peel stresses

It can be seen from Table 2 and Figs. 11 and 12 that, when the PZT smart beams are excited by the applied voltage, peel stresses are normally not equal to zero, and their peak values may be as large as or larger than those of the peak shear stresses. Eq. (67) in Part I (Tong and Luo, 2003) shows that, dynamic peel stress exists in the SLBM even though it is not taken into account in the original model.

When a structure vibrates at a relatively low frequency, the flexural motions are dominant. The flexural motions of PZT patch and host beam are different, particularly near the free PZT edge. When the peak peel

stresses are less than the dynamic peel strength of the adhesive, they prevent the PZT patch from peeling off from the parent structure. The existence of peel stresses provides an extra constraining effect for the smart structure and then increases the natural frequencies of the PZT smart structures. When the peak peel stresses are larger than the dynamic peel strength the PZT, debondings will be developed, which may eventually lead to loss of structural controllability.

Dynamic effects of shear stresses on smart structures are similar to those of peel stresses. It can be inferred that, the actuated shear and peel stresses do not only excited the parent structures, but also provide extra constraints. That is why, natural frequencies predicted by the exact solutions of PSM and SLRM are remarkably higher than those of the approximate solutions, and PSM gives higher natural frequencies than SLBM and SLRM.

The concept of the extra constraining effect induced by the shear and peel stresses also gives a good explanation to behaviors of dynamic debondings. It is known that an edge debonding can significantly decrease natural frequencies of a smart structure while an interior debonding does not. Kim and Jones (1996) also demonstrated this phenomenon in investigating the PZT actuated delamination. When the excitation frequency is low, the stresses concentrates near the PZT free edge, and hence the extra constraint can be relieved by an edge debonding and not an interior debonding. Seeley and Chattopadhyay (1998, 1999) concluded that the debonding length is a critical factor and an increase in debonding length introduces local and global deformations that have a significant effect on the mode shapes and frequencies, which is also verified by Tong et al. (2001) and Sun et al. (2001). As stress redistributions occur in the event of PZT edge debonding, a longer debonding causes more noticeable stress redistributions, which in turns affects the extra constraints, and then eventually affects the mode shapes and natural frequencies.

6.2. Dynamic balance

In static state, the shear and peel stresses for the free PZT ends are the balanced force system respectively. In dynamic analysis, if the inertia forces are included in the free body diagrams, the equations of the dynamic equilibrium can be set up following the procedure of the static equilibrium equations. In considering the dynamic balance of the PZT patch, the dynamic shear and peel stresses are no longer the balanced force system as existence of the axial and transverse inertial forces. The higher the excitation frequency, the larger the unbalanced excitation forces. Therefore, the approximate solutions are only applicable if the excitation frequency is low, even though the PZT patches are much thinner and shorter than the host beam.

7. Conclusions

The present exact dynamic solutions to PZT smart beams take into account peel stresses in adhesive and give more accurate results of frequency spectra, natural frequencies, normal mode shapes and dynamic responses.

The energy transfer stresses between PZT patches and parent structures do not only excite a smart structure but also provide extra constraints which lead to higher natural frequencies. In dynamic analysis of the PZT smart structures, peel stresses must be included in the PZT smart beam models, especially for flexible structures and debonding analysis.

When the PZT patches are much thinner and shorter than the host beam, approximate solutions of the shear lag models give reasonably accurate natural frequencies but not dynamic responses. The peel stress can only be neglected for the case of very thin and short PZT patches as well as low excited frequency.

In light of distributions of the peel stresses, the approximate solution procedure is developed by utilizing the present equivalent forces. The PZT patch mass and geometry and the coupled motions are also considered in the formulation. It provides better estimation for the quasi-static analysis.

Acknowledgements

The authors are grateful to the support of Australian Research Council through a Large Grant Scheme (grant no. A10009074), and to Dr. Dongchang Sun for sharing his numerical results obtained using the shooting method and helpful technical discussions.

References

Anderson, G.P., Bennett, S.J., De Vries, K.L., 1977. Analysis and Testing of Adhesive Bonds. Academic Press.

Crawley, E.F., Anderson, E.H., 1990. Detailed models of piezoceramic actuation of beams. J. Intelligent Material Systems and Structures 1, 4–25.

Crawley, E.F., de Luis, J., 1987. Use of piezoelectric actuators as elements of intelligent structures. AIAA J. 25 (10), 1373–1385.

Gibbs, G.P., Fuller, C.R., 1992. Excitation of thin beams using asymmetric piezoelectric actuators. J. Acoustic Soc. America 92 (6), 3221–3227.

Im, S., Atluri, S.N., 1989. Effects of a piezo-actuator on a finitely deformed beam subjected to general loading. AIAA J. 27 (12), 549–564.

Kim, S.J., Jones, J.D., 1996. Effects of piezo-actuator delamination on the performance of active noise and vibration control system. J. Intelligent Material Systems and Structures 7 (6), 668–676.

Lee, C.-K., 1992. Piezoelectric laminates: theory and experiments for distributed sensors and actuators. In: Tzou, H.S., Anderson, G.L. (Eds.), Intelligent Structural Systems. Kluwer Academic Publishers, pp. 75–135.

Luo, Q., Tong, L., 2002a. Exact static solutions to piezoelectric smart beams including peel stresses, Part I: Theoretical formulation. Int. J. Solids Struct. 39 (18), 4677–4695.

Luo, Q., Tong, L., 2002b. Exact static solutions to piezoelectric smart beams including peel stresses, Part II: Numerical results, comparison and discussion. Int. J. Solids Struct. 39 (18), 4697–4722.

Rizet, N., Brissaud, M., Gonnard, P., Bera, J.C., Sunyach, M., 2000. Modal control of beam flexural vibration. J. Acoustic Soc. America 107 (4), 2061–2067.

Seeley, C.E., Chattopadhyay, A., 1998. Experimental investigation of composite beams with piezoelectric actuation and debonding. Smart Materials and Structures 7, 502–511.

Seeley, E.C., Chattopadhyay, A., 1999. Modeling of adaptive composites including debonding. Int. J. Solids Struct. 36, 1823–1843.

Shi, G., Atluri, S.N., 1990. Active control of nonlinear dynamic response of space-frames using piezo-electric actuators. Computers and Structures 34 (4), 1801–1807.

Sun, D., Tong, L., Atluri, S.N., 2001. Effects of piezoelectric sensor/actuator debonding on vibration control of smart beams. Int. J. Solids Struct. 38, 9033–9051.

Tong, L., Luo, Q., 2003. Exact Dynamic solutions to piezoelectric smart beams including peel stresses, Part I: Theory and application. Int. J. Solids Struct., in press.

Tong, L., Steven, G.P., 1999. Analysis and Design of Structural Bonded Joints. Kluwer Academic, Boston.

Tong, L., Sun, D., Atluri, S.N., 2001. Sensing and actuating behaviors of piezoelectric layer in smart beams with debonding. Smart Materials and Structures 10 (4), 713–723.

Tylikowski, A., 2001. Effects of piezoactuator delamination on the transfer functions of vibration control systems. Int. J. Solids Struct. 38, 2189–2202.